Proceedings World Geothermal Congress 2015
Melbourne, Australia, 19-25 April 2015

Corrosion and Scaling in Habanero 4 Produced Fluids and 1 MWe Demonstration Plant

Ben Humphreys[1], Claus Christoffersen[1], Keith. A. Lichti[2], Jessica Wong[2], Monika Ko[2] and Robert Dudley[2]

[1]Geodynamics Ltd., PO Box 2046, Milton, Queensland, Australia

[2]Quest Integrity NZL Ltd., PO Box 38096, Lower Hutt, New Zealand

Ben.Humphreys@geodynamics.com.au K.Lichti@questintegrity.com

Keywords: EGC, geothermal, corrosion, carbon steel, low alloy steel, stainless steels, Ni-Base alloys

ABSTRACT

Corrosion tests run using geothermal brine derived from the Geodynamics well Habanero 4 in a high temperature, high pressure Engineered Geothermal System were completed in 2013. Preliminary results of these trials have been obtained for a range of engineering materials exposed in coupon form under actual production conditions. These results show a combination of CO_2 corrosion, H_2S corrosion and chloride pitting corrosion with occasional complications arising from heavy metal precipitation and galvanic corrosion. The test results provide input for future materials selection for reliable longer term EGS production trials at the Habanero site.

1. INTRODUCTION

Geodynamics completed a range of coupon exposure trials and heat exchanger trails as part of the 1 MWe Demonstration Plant EGS project. The coupon exposures were completed from 5 April 2013 to 31 October 2013 using brine produced from the Habanero 4 well with reinjection into the Habanero 1 well. Coupons were of a rolled ring design and positioned on a bar within 150 mm diameter pipes and insulated from the bar and from each other using ceramic spacers. The coupon alloys tested are described in Table 1.

The exposure locations are shown graphically in Figure 1 and approximate exposure test conditions summarised in Table 2, arranged by exposure dates. The samples were exposed for some time in air prior to testing and the samples experienced periods of no flow but remained with pressurised fluid at all times. Samples were promptly removed on completion of the testing.

Table 1: Coupon alloys tested.

Group 1: Carbon and Low Alloy Steels		Group 2: Stainless Steels and Ni-Base Alloys	
Alloy	**Description**	**Alloy**	**Description**
E235C	Seamless Cold Drawn Steel Tube	13CR	Casing, Tubing and Drill Pipe Steel
4130	1% Cr Steel	316L	Stainless Steel
A106B	Seamless Carbon Steel Pipe	718	Nickel Alloy
A182F11	1¼Cr-½Mo	6MO	Austenitic Stainless Steel
A182F22	2¼Cr-1Mo	2205	Duplex
		2507	Super Duplex

Table 2: Exposure conditions for coupons, arranged by exposure dates.

Location	Temperature, °C	Pressure, MPa	Flow Rate, kg/s	Flow Velocity, m/s	Exposure Dates (all in 2013)
A: After Wellhead	180 to 208	34	0 to 17	0 to 1.4	5 April to 18 May
A: After Wellhead	180 to 208	34	0 to 17	0 to 1.4	18 May to 13 August
B: Before Brine Heat Exchanger	180 to 208	34	0 to 17	0 to 1.4	5 April to 13 August
C: After Brine Heat Exchanger	145 to 188	34	0 to 17	0 to 1.4	5 April to 13 August
A: After Wellhead	210	34	1.5 to 19	0.1 to 1.6	13 August to 31 October
B: Before Brine Heat Exchanger	210 then 180	34	1.5 to 19	0.1 to 1.6	13 August to 31 October
C: After Brine Heat Exchanger	140	29 to 34	0 to 18	0 to 1.5	31 August to 24 September
D: After Brine Cooler	80	29 to 34	0 to 18	0 to 1.5	5 April to 31 August
D: After Brine Cooler	80	29 to 34	0 to 18	0 to 1.5	31 August to 12 October
E: After Brine Reinjection Pump	80	29 to 44	0 to 18	0 to 3.6	5 April to 31 August
E: After Brine Reinjection Pump	80	29 to 44	0 to 18	0 to 3.6	31 August to 24 September

2. EXPOSURE CHEMISTRY

The Habanero 4 fluids were sampled and downhole chemistry conditions reported by Brown (2012) as summarized in Table 3. This chemistry was used to model the cooling of the fluid from 250°C at a pressure of 399.3 bara with the aid of "WATCH24" (Arnorsson and Bjanrsason, 1993) and results given in Table 4.

Table 3: Habanero 4 well sample chemistry from Brown (2012).

Reservoir pH at 250 °C	6.03		
Sample collection point	LP		
Compound	**mg/L**	**Compound**	**mg/L**
Ammonia (liquid sample)	9.6	Rubidium	17.2
Antimony	2.44	Silica (as SiO_2)	497
Arsenic	1.88	Sodium	5140
Boron	253	Sulphate	63.0
Calcium	45.1	Carbon Dioxide (total)	8660
Cesium	39.5	Hydrogen Sulphide (total)	1.007
Chloride	8526	Argon	7.69
Fluoride	16.7	Helium	22.2
Iron	1.3	Hydrogen	0.0048
Lithium	243	Methane	1320
Magnesium	0.39	Nitrogen	701
Potassium	719		

Table 4: "Watch24" data used in corrosion process modeling.

Habanero 4 Corrosion Models							
Temperature	200°C	180°C	160°C	140°C	120°C	100°C	80°C
Total Pressure bar(a)	340.7	340.7	340.7	340.7	340.7	340.7	340.7
pCO_2 bar(a)	42.5	43.9	44.2	43.1	40.6	36.7	31.3
pH	5.493	5.307	5.14	4.994	4.873	4.779	4.717
pH_2 bara(a) *		1		1			1
Fe^{2+} (mol/kg) **		$1.00x10^{-5}$		$1.00x10^{-5}$			$1.00x10^{-5}$
Total CO2 (mol/kg)	0.424	0.424	0.424	0.424	0.424	0.424	0.424
Total S (mol/kg)	$4.57x10^{-4}$	$4.80x10^{-4}$	$5.01x10^{-4}$	$5.21x10^{-4}$	$5.39x10^{-4}$	$5.56x10^{-4}$	$5.72x10^{-4}$
Total S (mol/kg)	4.57E-04	$4.80x10^{-4}$	$5.01x10^{-4}$	$5.21x10^{-4}$	$5.39x10^{-4}$	$5.56x10^{-4}$	$5.72x10^{-4}$
Pourbaix Diagrams							
Fe-H_2S-H_2O		Figure 2		Figure 2			Figure 3
Fe-CO_2-H_2O				Figure 3			Figure 4

3. CORROSION COUPON RESULTS

Surface corrosion rates were obtained from mass change measurements made on the exposed coupons using the following equations from Braithwaite and Lichti (1981).

$$ML = \frac{\delta}{\rho A} \times 1000 \quad (1)$$

Where *ML, δ, ρ, A* are material loss in micrometers, weight loss in milligrams, density in mg/mm^3, and exposed area of test material in mm^2, respectively, and

$$CR = \frac{ML \times \text{constant}}{t} \quad (2)$$

Where *CR, ML, constant, t* are corrosion rate in micrometers per year, material loss in micrometers, 31 557 000 seconds per mean solar year, duration of exposure period in seconds, respectively.

Coupon corrosion results, analysis and observations are summarized in Table 5. The mass loss corrosion rates and pitting corrosion rates are given in Figure 7 through to Figure 10.

Table 5: Summary of coupon corrosion results, analysis and observations.

Location A – After Wellhead (180°C to 208°C)	**Group 1 Carbon and Low Alloy Steels**	**Group 2 Stainless Steels and Ni-Base Alloys**
5 April to 18 May	▪ Low to medium corrosion rates of the order 35 to 92 µm/year. ▪ Pitting rates of the order 195 to 1030 µm/year. ▪ XRF detected Sb and As with S, Fe and Cl in corrosion products ▪ XRD identified metallic Sb and stibnite (Sb_2S_3) on outer layers with underlying deposits of pyrrhotite ($Fe_{1-x}S$) and siderite ($FeCO_3$)	▪ Very low corrosion rates (except 316L and 13CR) of the order 0.2 to 1.2 µm/year. ▪ 316L had slightly higher corrosion rates of the order 0.5 to 2.0 µm/year. ▪ 13CR had low corrosion rates of the order 8.3 to 17.4 µm/year and pitting rates of the order 45 to 187 µm/year. ▪ Corrosion product and scale XRF analysis showed very low levels of Sb and As. S, Fe, Si and Cl were also detected
18 May to 13 August	▪ Medium to high corrosion rates of the order 88 to 112 µm/year ▪ Pitting rates of the order 110 to 217 µm/year ▪ XRF detected Sb and As with S, Fe and Cl in corrosion products. ▪ SEM-EDX analysis confirmed the presence of Sb and As, as well as Fe and S and showed the distribution of pyrrhotite ($Fe_{1-x}S$) and pyrite (FeS_2). Oxygen was also present suggesting magnetite (Fe_3O_4). ▪ Optical microscopy showed layers of iron sulfides, iron oxides and iron carbonates.	
13 August 2013 to 31 October 2013	▪ Low corrosion rates of the order 30 to 57 µm/year. ▪ Pitting corrosion rates of the order 70 to 210 µm/year. ▪ XRF analysis on the top surface scales indicated sulfur was present on all surfaces analysed and this sulfur is balanced with iron and arsenic but not with antimony. Trace amounts of Cl were also detected. ▪ XRD analysis indicated siderite ($FeCO_3$), pyrrhotite ($Fe_{1-x}S$) and magnetite (Fe_3O_4). ▪ Optical microscopy confirmed the presence of siderite ($FeCO_3$) and magnetite (Fe_3O_4). Iron-chromium spinel was also detected	▪ Very low corrosion rates of the order 0.3 µm/year, except for 316L and 13CR. ▪ 316L had a very low corrosion rate of the order 1.25 µm/year ▪ 13CR had a low corrosion rate of the order 20 µm/year. ▪ 13CR pitting corrosion rate of the order 260 µm/year. ▪ XRF results indicated the deposits were thin (as indicated by the XRF beam penetrating to base metal i.e. XRF beam penetrates 50µm into surface) and mainly deposited from solution, being enhanced in sulfur and "Bal" i.e. elements lighter than magnesium
Location B – Before Brine Heat Exchanger (180°C to 208°C)	**Group 1 Carbon and Low Alloy Steels**	**Group 2 Stainless Steels and Ni-Base Alloys**
5 April to 13 August	▪ Low to medium corrosion rates of the order 39 to 66 µm/year. ▪ Pitting rates of the order 160 to 630 µm/year. ▪ XRF analysis detected Sb and As with Fe, S, Si and trace levels of Cl ▪ XRD identified a magnetite like spinel Fe3O4, siderite ($FeCO_3$) and pyrrhotite ($Fe_{1-x}S$) after partial chemical cleaning of outer layers. ▪ SEM-EDX analysis confirmed the presence of As and Sb as well as Fe, S and Cr reflecting pyrrhotite ($Fe_{1-x}S$), pyrite (FeS_2) and iron chrome spinel. ▪ Optical microscopy of scales after an initial chemical clean found layers of iron oxide that were occasionally rich in chromium, silica was also detected.	▪ Very low corrosion rates (except 316L and 13CR) of the order 0.3 to 0.8 µm/year. ▪ 316L had a low corrosion rate of the order 3.6 µm/year. ▪ 13CR had a low corrosion rate of the order 8.9 µm/year and a pitting rate of the order 87 µm/year. ▪ XRF analysis detected low levels of Sb and As with S, Fe, Si and Cl were also detected in corrosion products.
13 August to 31 October	▪ Low to medium corrosion rates of the order 32 to 69 µm/year. ▪ Pitting corrosion rates of the order 90 to 350 µm/year. ▪ XRF analysis on the top surface scales indicated sulfur was present on all surfaces analysed and this sulfur is balanced with iron and arsenic but not with antimony. Trace amounts of Cl were also detected. ▪ XRD analysis on the surface indicated	▪ Very low corrosion rates of the order 0.4 µm/year except 13CR. ▪ 13CR had a low corrosion rate of the order 24.8 µm/year. ▪ 13CR had a pitting corrosion rate of the order 450 µm/year. ▪ XRF results indicated the deposits were thin (as indicated by the XRF beam penetrating to base metal i.e. XRF beam penetrates 50µm into surface)

	amorphous phase and some crystalline Sb compounds. ▪ Optical microscopy of the cross section indicated magnetite (Fe3O4) and iron-chromium spinel.	and mainly deposited from solution, being enhanced in sulfur and "Bal" i.e. elements lighter than magnesium
Location C – After Brine Heat Exchanger (145°C to 188°C)	**Group 1 Carbon and Low Alloy Steels**	**Group 2 Stainless Steels and Ni-Base Alloys**
5 April to 13 August	▪ Low to medium corrosion rates of the order 34 to 101 µm/year. ▪ Pitting rates of the order 160 to 630 µm/year. ▪ XRF analysis detected Sb and As at levels similar to that of the early exposure in Location A. Fe, S, Si and trace levels of Cl were also detected. ▪ XRD identified metallic Sb and stibnite (Sb_2S_3) on outer layers. ▪ SEM-EDX analysis confirmed the presence of Sb, S and As, with SEM images showing the presence stibnite.	Not exposed at this location
31 August to 24 September	▪ High corrosion rates of the order 300 µm/year. ▪ Pitting corrosion rates of the order 837 to 1430 µm/year. ▪ XRF analysis showed Sb and S at high levels with Fe and a significant Balance (assumed C and O). Low levels of As and Cl were also seen.	
Location D - After Brine Cooler (80°C)	**Group 1 Carbon and Low Alloy Steels**	**Group 2 Stainless Steels and Ni-Base Alloys**
5 April to 31 August	▪ Medium to high corrosion rates of the order 42 to 240 µm/year. ▪ Pitting corrosion rates of the order 200 to 965 µm/year. ▪ XRF analysis on these coupons showed enhanced As and low level Sb with Fe and S and occasional Cl.	▪ Very low corrosion rates of the order 0.1 to 2.5 (13CR) µm/year. ▪ Pitting corrosion rate for 13CR of the order 200 um/year. ▪ XRF analysis showed enhanced As and low level Sb with Fe and S and occasional Cl.
31 August to 12 October	▪ All Group 1 coupons except for E235C showed high corrosion rates of the order 180 to 760 µm/year. ▪ E235C had a very high erosion corrosion rate greater than 3000 µm/year. ▪ Pitting corrosion rates were of the order 1900 µm/year. ▪ XRF analysis on these coupons showed enhanced As and low level Sb. Fe, S and occasional Cl were also detected. ▪ XRD analysis on the E235C alloy characterised the deposit compounds as troilite (FeS), siderite ($FeCO_3$), pyrrhotite ($Fe_{1-x}S$), cohenite (Fe_3C) and cristobolite (SiO_2). ▪ Optical Microscopy indicated siderite ($FeCO_3$), pyrrhotite ($Fe_{1-x}S$) and realgar (As_4S_4) on exposed A106B alloy.	
Location E - After Brine Reinjection Pump (80°C)	**Group 1 Carbon and Low Alloy Steels**	**Group 2 Stainless Steels and Ni-Base Alloys**
5 April to 31 August and 31 August to 12 October	▪ All alloys (except for E235C) had medium to high corrosion rates of the order 80 to 200 µm/year ▪ All alloys (except for E235C) had pitting corrosion rates of the order 340 to 550 µm/year. ▪ E235C had a very high erosion corrosion rate greater than 10300 µm/year. ▪ XRF analysis showed enhanced As and low level Sb. Fe, S and Cl were also detected. ▪ XRD analysis characterised these compounds on the A182F22 alloy exposed as realgar (As_4S_4), alacranite (As_4S_4), halite (NaCl) and quartz (SiO_2). ▪ Optical microscopy characterised the compounds on the severely corroded and eroded E235C alloy as siderite ($FeCO_3$), pyrrhotite ($Fe_{1-x}S$), realgar (As_4S_4).	▪ All coupons (except 13CR) showed very low corrosion rates of the order 0.1 to 1.2 µm/year. ▪ 13CR had low corrosion rates of the order 2 to 25 µm/year. ▪ 13CR had pitting corrosion rates of the order 180 to 290 µm/year. ▪ XRF analysis showed enhanced As and low level Sb. Fe, S and Cl were also detected.

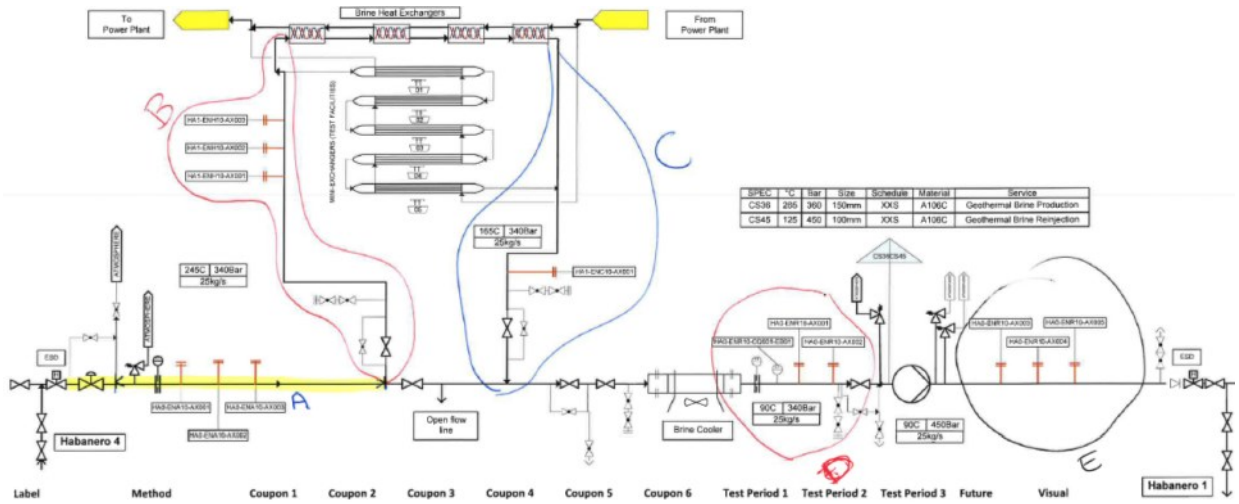

Figure 1: Coupon exposure locations.

4. CORROSION MODELS

The corrosion processes and corrosion rates were modelled using Potential-pH Pourbaix type diagrams for corrosion in the Fe-H_2S-H_2O and Fe-CO_2-H_2O systems and calculations of CO_2 corrosion as a function of measured and estimated parameters. Effect of chloride with respect to onset of localised corrosion was also addressed. Models for heavy metal deposition and galvanic corrosion were considered.

4.1 Potential-pH Pourbaix Diagrams

A methodology for the preparation of corrosion product stability potential-pH Pourbaix type diagrams has been described by, for example, Chen and Aral (1983). The software provided by these authors in particular has been implemented by Quest Integrity in an automated system requiring input of thermodynamic data and chemistry conditions for the desired modelling. A database of thermodynamic properties of iron compounds has been developed for this work from a number of different sources. The database has been proven effective in a range of New Zealand, Philippines, Indonesian and Japanese geothermal systems for high temperature geothermal steam and brine environments; see for example Lichti *et al*. (1997).

Selected data from the "WATCH24" calculations for cooled fluid from 200°C to 80°C was used as input for calculation of corrosion product stability diagrams (as a means of inferring corrosion rates) and for estimation of CO_2 corrosion rates as a function of partial pressure CO_2 (pCO_2), temperature and other factors, see Table 4.

Pourbaix diagrams were prepared for a Fe-H_2S-H_2O system at 180°C, 140°C and 80°C as given in Figure 2 and Figure 3. Pourbaix diagrams were prepared for a Fe-CO_2-H_2O system at 140°C and 80°C as given in Figure 3 and Figure 4. Two values for Fe^{2+} in solution were used for the 80°C models.

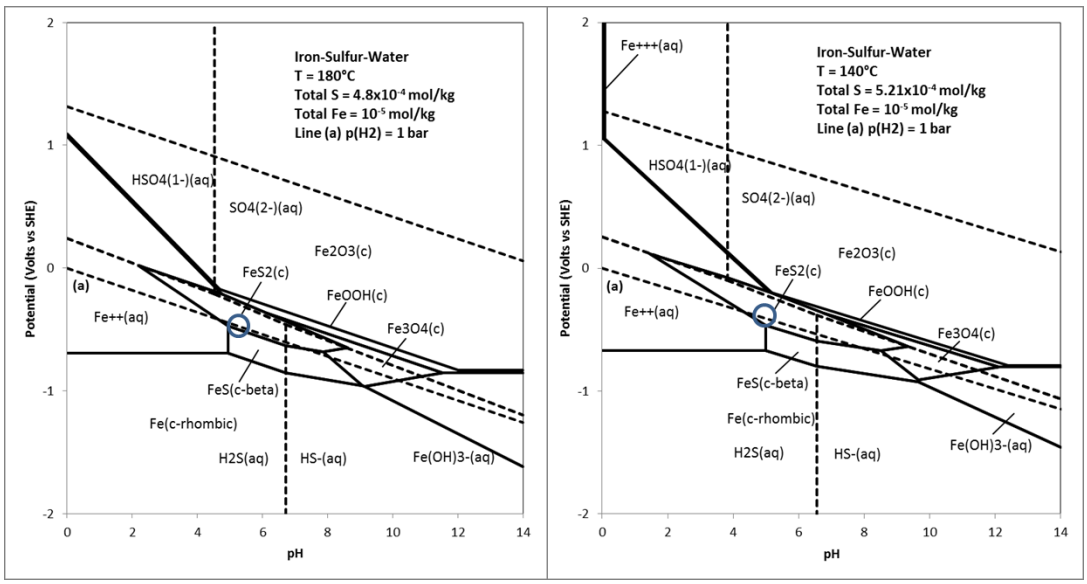

Figure 2: Potential-pH Pourbaix diagram for Fe-H_2S-H_2O steam chemistry at 180°C and 140°C.

4.2 CO_2 and H_2S Corrosion Rate Models

A number of methodologies for the prediction of CO_2 corrosion are available, Quest Integrity use a model based on that proposed by deWaard and Lotz (1994) with enhancements for high pressures of CO_2 from Seiersten (2000) and adjustments for H_2S based on results from Lee (2004). The model has been developed as illustrated in Figure 5 for temperatures higher than 120°C and for temperatures lower than 120°C. The 120°C division is proposed due to changing chemistry from high to low temperatures, pCO_2 decreases as the temperature decreases and pH decreases as temperature is lowered. The lowering of pH gives increased stability of Siderite.

Application of the additional factor for H_2S corrosion product formation in the model using the data of Lee (2004) successfully matches the apparent suppression of CO_2 corrosion observed in this work, see Figure 5.

The Pourbaix diagrams for Fe-H_2S-H_2O show that iron sulfides, Pyrrhotite and Pyrite, are the dominant phases that form and these phases were demonstrated as stable in the Habanero fluids on carbon and low alloy steels. These phases, once formed, can block the corrosive solution from the environment and iron oxides can form next to the metal surface. This same process was demonstrated to be occurring in the Habanero 4 high temperature fluids in cross sections with the complication that both iron oxide and iron carbonate are both observed under the iron sulfide layers.

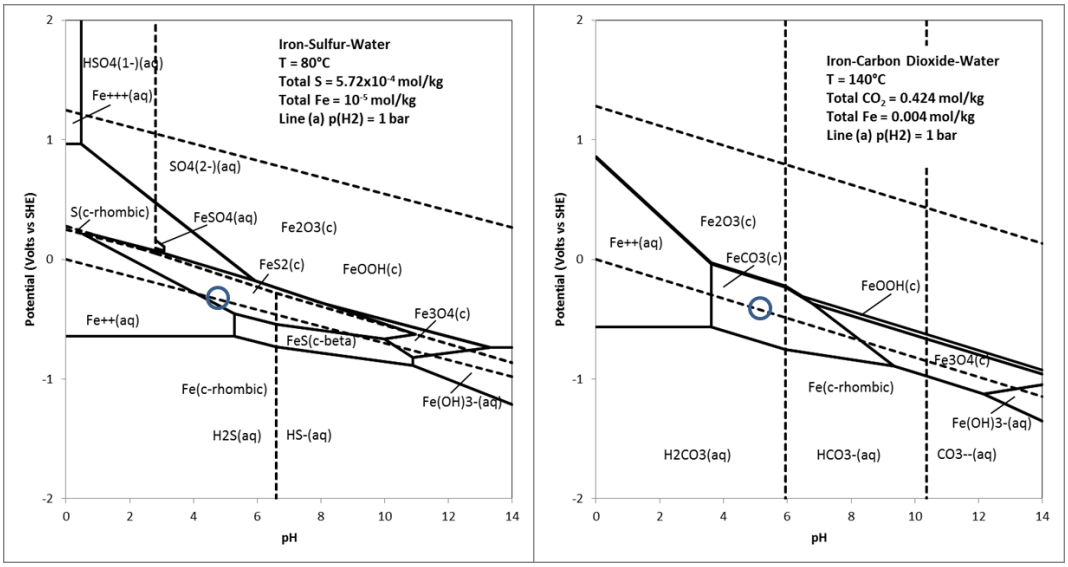

Figure 3: Potential-pH Pourbaix diagram for Fe- H_2S-H_2O steam chemistry at 80°C and for Fe-CO_2-H_2O steam chemistry at 140°C with high iron

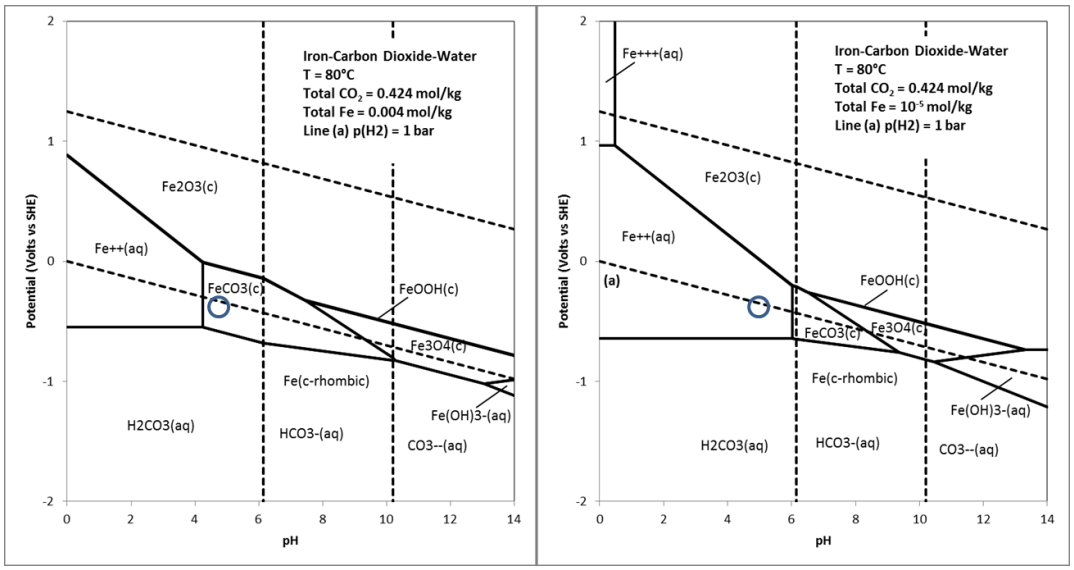

Figure 4: Potential-pH Pourbaix diagram for Fe-CO_2-H_2O steam chemistry at 80°C with high iron (left) and reported iron (right)

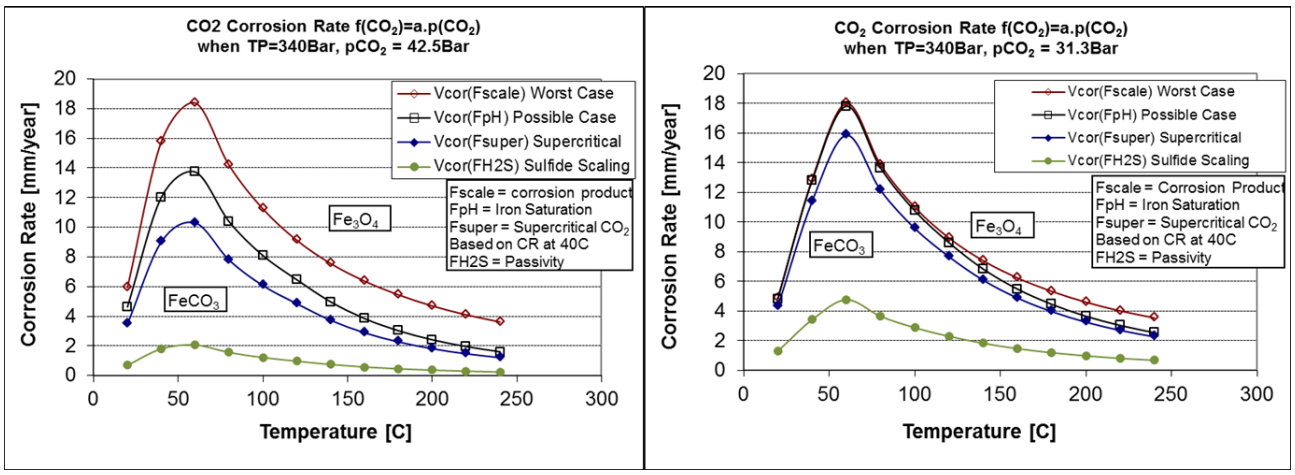

Figure 5: CO_2 corrosion rate nomogram valid for temperatures greater than 120°C (left) and temperatures less than 120°C (right). CO2 Corrosion based on de Waard and Lotz (1994) with enhancements from Seiersten (2000) for high partial pressure of CO_2 and from Lee (2004) for H_2S corrosion.

Lower temperature geothermal fluids (less than 80°C) have been shown to require extended time to form protective films and in some instances, for example under high flow and low Fe^{2+} in solution, protective scales may not form. This is demonstrated in Figure 6.

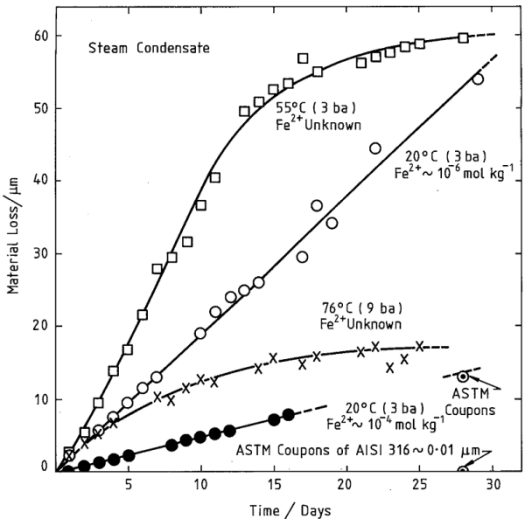

Figure 6: Quest Integrity data for H2S corrosion in steam condensate as a function of temperature and dissolved iron, Lichti and Julian (2010)

The Pourbaix diagrams for Fe-CO_2-H_2O demonstrate that with reducing effect of H_2S, iron carbonate stability is achieved but this is dependent on iron concentration used for preparation of the diagrams, see Figure 4. At high concentrations of iron, iron carbonate stability is achieved through low pH values (pH < 4) whereas at low concentrations of iron, free corrosion would be predicted (pH < 6).

These diagrams suggest that Location D, for example with a lower flow velocity than Location E, has less risk of erosion corrosion. The rate of erosion corrosion in high velocity fluids at 80°C might be of the order 4 mm/year with H_2S making a strong contribution to corrosion control. Without H_2S corrosion control, the erosion corrosion rate might be of the order 12 mm/year.

5. SUMMARY OF CORROSION DAMAGE MECHANISMS

5.1 Location A - After Wellhead

Coupons experienced temperatures in the range 180 to 210°C. Multiple exposures were completed and the results were generally consistent. Process conditions at Location A were unsteady for a significant time during the first exposure period (5 April to 18 May) and at a lower average temperature during the second exposure period (18 May to 13 August) - corrosion rates were lower and pitting rates higher in the first exposure period compared with the second. The effect of temperature, which varied, is difficult to factor into any estimate of corrosion rate as both CO_2 corrosion and H_2S corrosion may increase as temperature is lowered. The key corrosion and corrosion damage mechanisms were:

Carbon and Low Alloy Steels

Carbon and low alloy steels occasionally showed presence of elemental Sb (elemental As was not seen but is also expected). This was accompanied by localised corrosion that suggested the corrosion process had some potential for reductive deposition of heavy metal scale followed by localised under layer corrosion enhanced by galvanic corrosion. The presence of iron oxide (and iron

chrome spinels), iron carbonate and iron sulfide indicated a complex corrosion process, including contribution from H_2S and CO_2 corrosion. There was some variability in the results from repeated exposures and this may be related to exposure variations including temperature, present or absence of heavy metal deposition, standby periods. There was no evidence of erosion corrosion in this test which included extended periods of time at a flow velocity of the order 1.6 m/s.

The corrosion damage mechanisms included:

- H_2S corrosion and CO_2 corrosion at low levels in the high temperature fluids.
- Localised pitting corrosion, at times clearly associated with heavy metal deposition and galvanic corrosion but mainly attributable to the chloride at 8,500 ppm

The predictive models show:

- The observed pitting rates match the model for CO_2 corrosion data of Shannon (1977) with a strong effect of pH, supercritical pressure and presence of H_2S.
- The localised corrosion observed matches the data of Shannon (1977) for a 1% NaCl in CO_2-bicarbonate brines at high temperature.
- The Pourbaix diagram for Fe-H_2S-H_2O of Figure 2 is considered to dominate the corrosion with iron sulfide formation and underlying iron oxide and minor indications of siderite stability.
- Reductive deposition of heavy metal scale is having some impact on the rate of pitting corrosion that is difficult to quantify

Stainless Steels and Ni-Base Alloys

The performance of these alloys (except 13CR) was acceptable and suggests good passive film formation. There was no erosion corrosion and no indication of localised corrosion (except for 13CR). 13CR was the worst performing alloy in this group and showed low corrosion rates with the corrosion dominated by localised corrosion, indicating some effect of chloride in film breakdown. Alloy 316L was susceptible to surface corrosion at a low level.

The corrosion damage mechanisms included:

- Presumed formation of iron-chrome spinels and observed localised corrosion on 13CR alloy.
- Formation of thin passive films on the remaining stainless steels and Ni-Base alloys with no onset of localised corrosion.
- No standby corrosion was indicated (good exclusion of oxygen at low flow conditions).

5.2 Location B - Before Brine Heat Exchanger

Coupons experienced temperatures in the range 180 to 208°C. The conditions were similar to those at Location A. There was a strong tendency to localised corrosion indicating some effect of chloride in contributing to film breakdown. Corrosion products and scales in their as received condition were not analysed in detail, however the presence of iron sulfides and iron carbonates indicates contribution from H_2S and CO_2 corrosion. The key corrosion and corrosion damage mechanisms were:

Carbon and Low Alloy Steels

There was no clear distinction between the performances of the different alloys in this group at this location. Very similar results to Location A were observed with reference to corrosion products present and pitting rates. There was no evidence of erosion corrosion in this test which included extended periods of time at a flow velocity of the order 1.6 m/s. The corrosion damage mechanisms were similar to those at Location A.

Stainless Steels and Ni-Base Alloys

The performance of these alloys (except 13CR) was acceptable and suggests good passive film formation. There was no erosion corrosion and no indication of localised corrosion (except for 13CR). 13CR was the worst performing alloy in this group with the corrosion rate being dominated by localised corrosion, indicating some effect of chloride in film breakdown. Alloy 316L was the second worst performer. These results were similar to Location A. The corrosion damage mechanisms were similar to those at Location A.

5.3 Location C – After Brine Heat Exchanger

Coupons experienced temperatures of the order 140°C. Corrosion rates were slightly higher than Location B and of a similar magnitude to Location A but pitting rates were higher than for the higher temperature locations. Elemental antimony and stibnite were identified by XRD in outer layers. The key corrosion and corrosion damage mechanisms were:

Carbon and Low Alloy Steels

The confirmed presence of elemental Sb (elemental As was not seen but is also expected) on the outer coupon surfaces following exposure together with the localised pitting corrosion results suggests that the corrosion process had some potential for reductive deposition of an outer layer of heavy metal scale followed by localised under layer corrosion enhanced by galvanic corrosion. Detailed cross section analysis of scales was not undertaken, however, the occasional presence of iron sulfides indicates contribution from H_2S corrosion. It is likely there was some effect of H_2S as well as CO_2 corrosion at this location. There was no evidence of erosion corrosion in this test which included extended periods of time at a flow velocity of the order 1.6 m/s. Localised corrosion is present indicating some effect of chloride in contributing to film breakdown.

The corrosion damage mechanisms included:

- H_2S corrosion and CO_2 corrosion at low levels in the high temperature fluids.

- Localised pitting corrosion, possibly associated with heavy metal deposition and galvanic corrosion but mainly attributable to the chloride at 8,500 ppm.

The predictive models show:

- The observed pitting rates match the model for CO_2 corrosion in Figure 5 with a strong effect of pH, supercritical pressure and presence of H_2S.
- The localised corrosion observed matches the increasing magnitude of pitting corrosion suggested by Shannon (1977) as the temperature is lowered for 1% NaCl in CO_2-bicarbonate brines.
- The Pourbaix diagram for Fe-H_2S-H_2O of Figure 2 is considered to be less dominant than that for Fe-CO_2-H_2O of Figure 3 as Siderite is becoming more prevalent than the iron sulfides.
- Reductive deposition of heavy metal scale is having some impact on the rate of pitting corrosion and is difficult to quantify.

5.4 Location D – After Brine Cooler

Coupons experienced temperatures of the order 80°C. Corrosion rates were slightly enhanced over Location D and pitting rates were higher than for all of the higher temperature locations. Elemental antimony was not identified by XRD which showed iron sulfides, iron carbonate, iron carbide and some silica. The presence of iron carbide and a predominance of iron carbonate were demonstrated in cross sections. Onset of erosion corrosion was observed on several materials. The key corrosion and erosion corrosion damage mechanisms were:

Carbon and Low Alloy Steels

Pitting corrosion rates of the order 1 mm/year were observed. There was evidence of erosion corrosion in this test of the order 1.9 mm, which included extended periods of time at a flow velocity of the order 1.5 m/s. The pitting and erosion was accompanied by iron carbonate stability indicating CO_2 corrosion contributed significantly to the corrosion damage process. The occasional presence of iron sulfides indicates some contribution from H_2S corrosion.

The corrosion damage mechanisms included:

- CO_2 corrosion and H_2S corrosion with CO_2 corrosion dominating under erosion corrosion conditions in the low temperature fluids.
- Localised pitting corrosion, mainly attributable to the chloride at 8,500 ppm.

The predictive models show:

- The observed pitting rates match the model for CO_2 corrosion suggested by Shannon (1977) with a strong effect of pH, supercritical pressure and presence of H_2S.
- The localised corrosion observed matches the increasing magnitude of pitting corrosion suggested by Shannon (1977) for 1% NaCl in CO_2-bicarbonate brines as the temperature is lowered.
- The Pourbaix diagram for Fe-H_2S-H_2O of Figure 3 is much less dominant than that for Fe-CO_2-H_2O of Figure 4 as Siderite is the prevalent corrosion product formed.

Stainless Steels and Ni-Base Alloys

The performance of these alloys (except 13CR) was acceptable and suggests good passive film formation. There was no erosion corrosion and no indication of significant corrosion (except for 13CR). 13CR was the worst performing alloy in this group with the corrosion rate being dominated by localised corrosion, indicating some effect of chloride in film breakdown. The pitting of 13CR was less than at Location A and Location B.

The corrosion damage mechanisms included:

- Presumed formation of iron-chrome spinels and observed localised corrosion on 13CR alloy, with the lower rate consistent with the expected improved resistance of 13CR type alloys to CO_2 corrosion as the temperature is decreasing from 150°C, Ikeda and Ueda (1994).
- Formation of thin passive films on the remaining stainless steels and Ni-Base alloys with no onset of localised corrosion.
- No standby corrosion was indicated (good exclusion of oxygen at low flow conditions).

5.5 Location E – After Brine Reinjection Pump

Coupons experienced temperatures of the order 80°C. One significant variation for this location compared to Locations A, B, C and D was the increase in the flow velocity with the reduction of the pipeline internal diameters from 120 mm to 100 mm. The grain structure of the E235C alloy was determined to be equiaxed i.e. equal dimensions in all directions and extremely susceptible to erosion corrosion. Other alloys also showed end grain breakdown and onset of severe erosion corrosion.

Carbon and Low Alloy Steels

There was evidence of erosion corrosion in this test which included extended periods of time at a flow velocity of the order 3.6 m/s. Siderite ($FeCO_3$) was readily detected indicating some contribution from CO_2 corrosion. The occasional presence of iron sulfides indicates some contribution from H_2S corrosion. Alloy A182F22 had the lowest corrosion rate following the testing, however pit depths measured on this alloy were still quite severe.

The corrosion damage mechanisms included:

- CO_2 corrosion and H_2S corrosion with CO_2 corrosion dominating under erosion corrosion conditions in the low temperature fluids.
- Localised pitting corrosion, mainly attributable to the chloride at 8,500 ppm.

The predictive models show:

- The erosion corrosion observed matches the increasing magnitude of corrosion in the absence of passivating effect of H_2S, as shown in Figure 5.
- The Pourbaix diagrams for Fe-CO_2-H_2O of Figure 4 at 80°C that shows Siderite stability as a function of iron concentration provide insight into the reason for the onset of erosion corrosion – poorly protective iron carbonate formation under low iron and close to the border with free corrosion (Fe^{2+} region).

Stainless Steels and Ni-Base Alloys

The performance of these alloys was acceptable and suggests good passive film formation. There was no erosion corrosion and no indication of localised corrosion (except 13CR). This indicated the maintenance of pressure and low flow on the system provided effective exclusion of oxygen and avoided onset of standby/shutdown corrosion on these alloys that are susceptible pitting and crevice corrosion under stagnant aerated conditions. 13CR was the worst performing alloy and showed localised corrosion at a low density, potentially due to CO_2 corrosion.

The corrosion damage mechanisms included:

- Presumed formation of iron-chrome spinels and observed localised corrosion on 13CR alloy up to 0.3 mm/year.
- Formation of thin passive films on the remaining stainless steels and Ni-Base alloys with no onset of localised corrosion.

6. CONCLUSIONS

The carbon and low alloy steel corrosion rates were strongly dependent on the location and conditions in the 1 MWe demonstration plant. The higher temperature locations A and B (of the order 180°C) show a strong effect of H_2S and CO_2 in promotion of protective corrosion product layers of iron sulfides and iron oxides. Localised corrosion was seen and attributed either to heavy metal scaling and galvanic corrosion or to chloride induced pitting corrosion at a level where a corrosion allowance can be selected to allow economic use of these lower priced materials, for example, for produced brine gathering pipelines from a number of wells. Location C at the lower temperature of 140°C shows increased corrosion and pitting rates that may limit the use of carbon and low alloy steels as increased corrosion allowances are required.

The low temperature, 80°C, conditions at Locations D and E show greater effect of CO_2 corrosion with onset of erosion corrosion at Location C where the flow velocity was increased to 3.6 m/sec compared to 1.5 m/sec at Location D. The flow velocity was seen as a major design change requirement for future plant.

Corrosion and erosion corrosion models were developed to describe the principal damage mechanisms and the observed rates of damage accumulation matched with published data for similar environments.

REFERENCES

Arnorsson, S., and Bjanrsason, J.O.: WATCH, Science Institute Orkustofnun, University of Iceland, Reykjavik, Iceland (1993).

Braithwaite, W. R and Lichti, K. A.: Surface Corrosion of Metals in Geothermal Fluids, New Zealand, in *Geothermal Scaling and Corrosion, ASTM STP 717*. L A Casper and T R Pinchback, Eds, ASTM, 1980, pp 81-112. (1981)

Brown, K.: Habanero 4 Chemistry, GEOKEM, Christchurch (2012).

Chen, C. M. and Aral, K.: Computer-Calculated Potential pH Diagrams to 300°C, EPRI NP-3137 Project 1167-2, Vols. 1, 2 and 3. (1983).

Ikeda, A., and Ueda, M.: CO_2 Corrosion Behaviour of Chrome Containing Steels, *Predicting CO_2 Corrosion in the Oil and Gas Industry*, European Federation of Corrosion Publications No. 13, The Institute of Materials (1994).

Lee, K. J.: A Mechanistic Modelling of CO_2 Corrosion of Mild Steel in the Presence of H_2S, Doctoral Thesis, Department of Chemical Engineering, Ohio University (2004).

Lichti, K.A., Inman, M.E., and Wilson, P.T.: Corrosivity of Kawerau Geothermal Steam," *Transactions- Geothermal Resources Council*, **21**, (1997) 25-32.

Lichti, K.A., and Julian, R.J.: Corrosion and Scaling in High Gas (25wt%) Geothermal Fluids, *Proceedings*, World Geothermal Congress, Bali (2010).

Seiersten, M.: Corrosion of Pipeline Steel in Supercritical CO_2 / water mixtures, *Proceedings,* EuroCorr2000, London (2000).

Shannon, D.W.: Corrosion of Iron-base Alloys Versus Alternate Materials in Geothermal Brines, Interim Report – Period Ending October 1977, Battelle, Pacific Northwest Laboratories, Richland, WA (1977).

de Waard, C., and Lotz, U.: Prediction of CO_2 Corrosion of Carbon Steel, *Predicting CO2 Corrosion in the Oil and Gas Industry*, European Federation of Corrosion Publications No. 13, The Institute of Materials (1994).

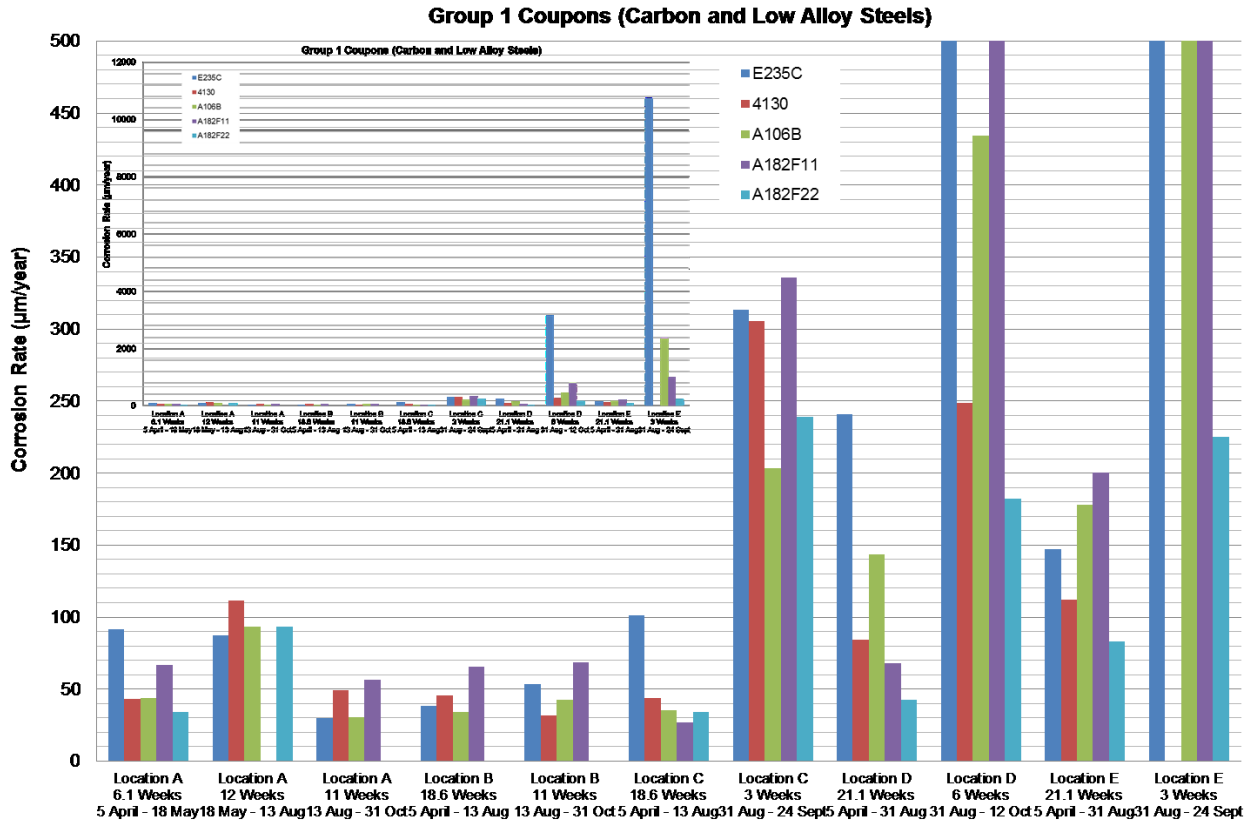

Figure 7: Corrosion rates of Group 1 Carbon and Low Alloy Steel coupons. Blank areas indicate coupons that were retained for destructive testing.

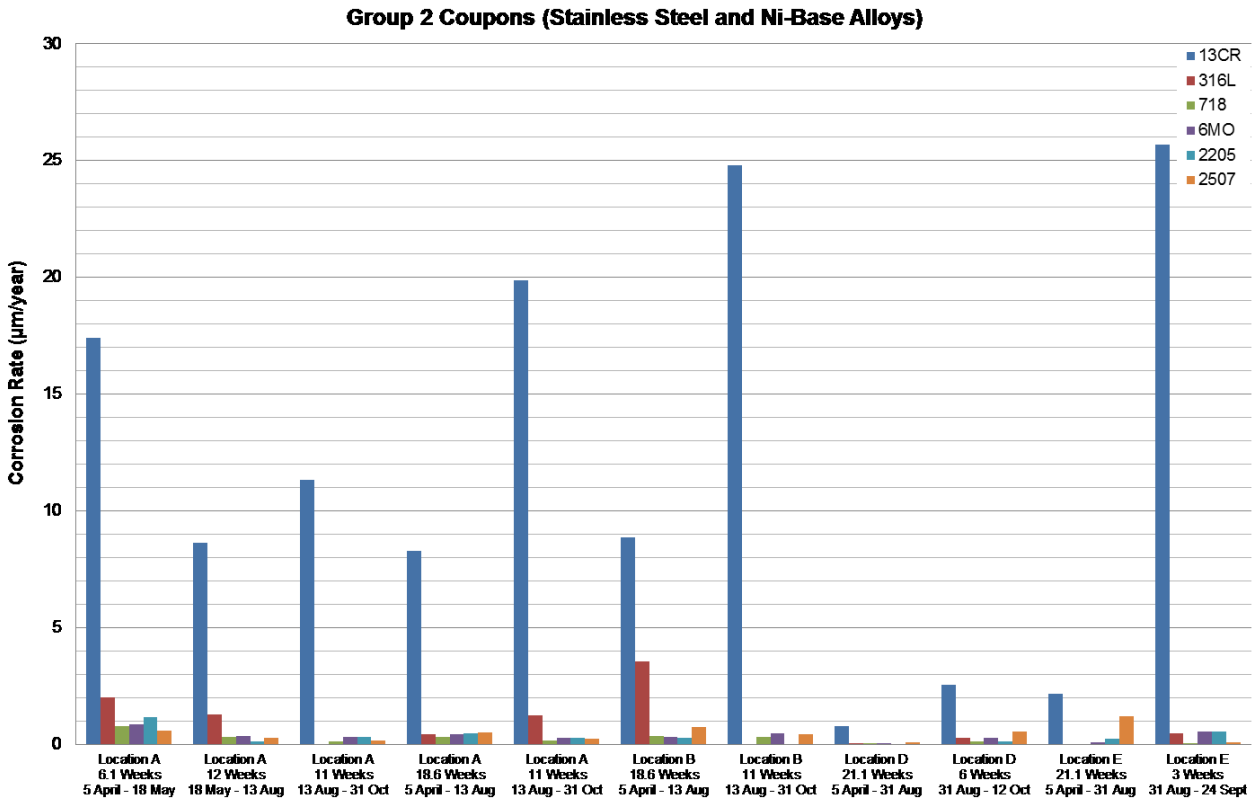

Figure 8: Corrosion rates of Group 2 Stainless Steels and Ni-Base alloy coupons.

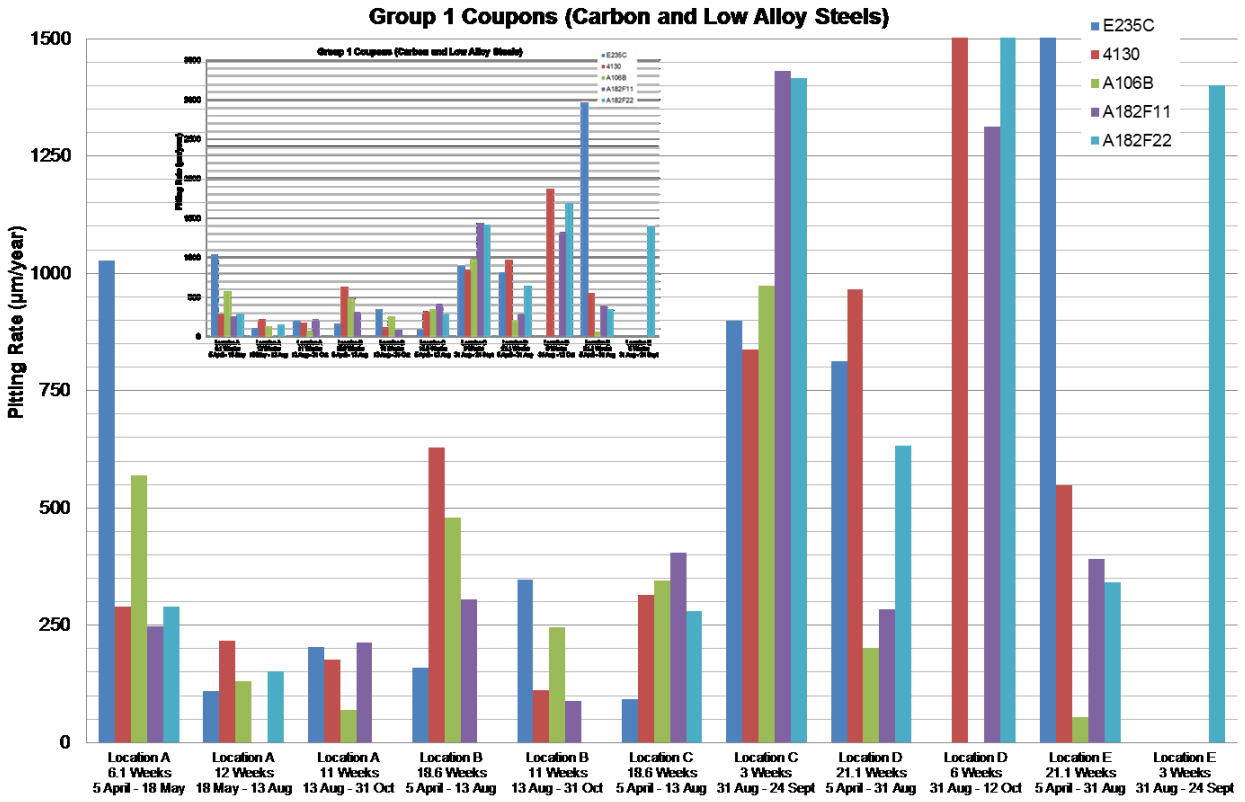

Figure 9: Pitting rate results for exposed Carbon and Low Alloy Steel coupons. Blank areas indicate coupons were retained for destructive testing and not measured

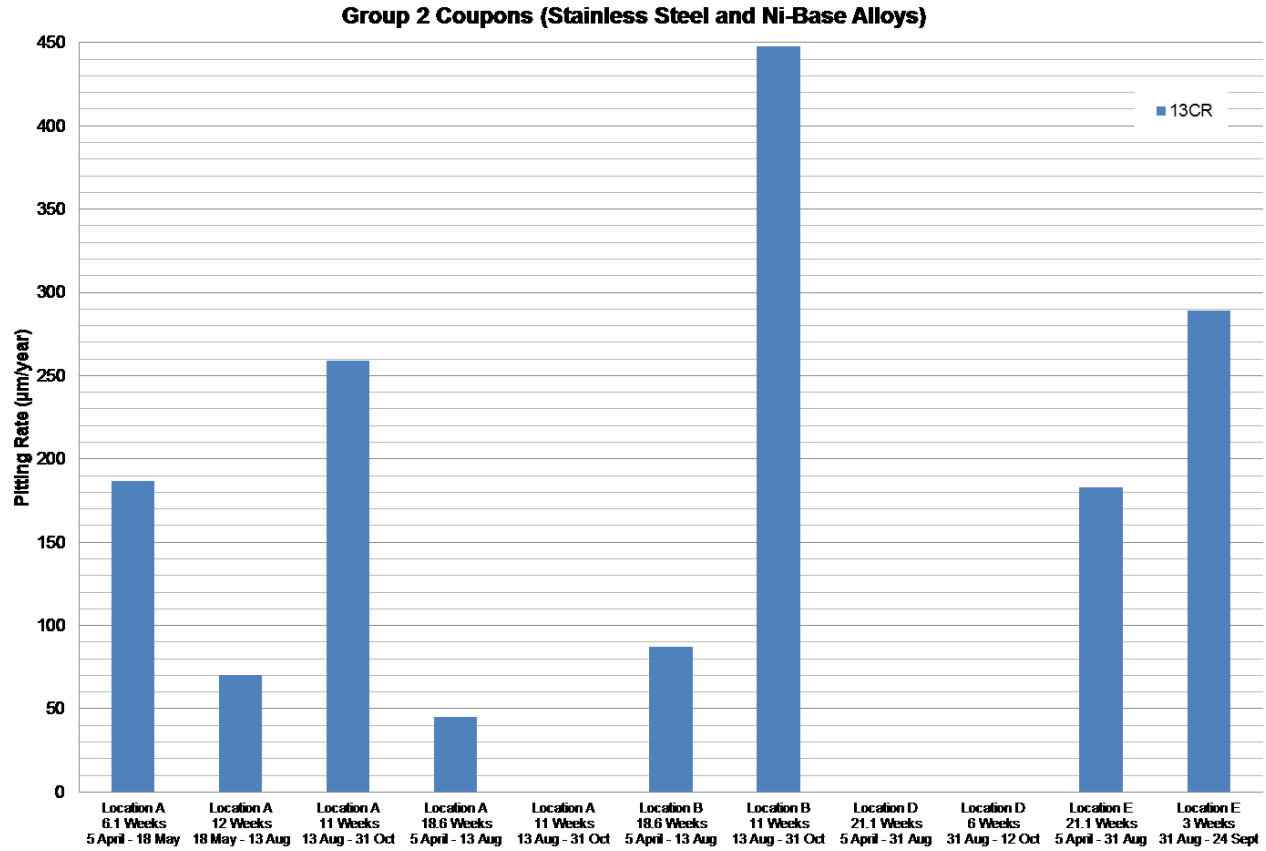

Figure 10: Pitting rate results for exposed 13CR alloys from Group 2 Stainless Steels and Ni-Base alloys. Blank areas indicate areas where no pitting was observed after exposure. Pitting was not observed on the rest of the exposed Group 2 coupons.